

PERMEABILITY ANALYTICAL MODELING OF 3D INTERLOCK FABRICS

N. Vernet* and F. Trochu

Department of Mechanical Engineering, Chair on Composites of High Performance (CCHP),
Centre de Recherche sur les Polymères et Composites à haute performance (CREPEC),
École Polytechnique de Montréal, Station Centre Ville, Montréal, Canada, H3C 3A7

* Corresponding author (nicolas.vernet@polymtl.ca)

Keywords: permeability, 3D fabric, modeling

1. General Introduction

Liquid Composite Molding (LCM) processes are increasingly used to manufacture composite parts in various areas such as the aerospace, automotive or marine industries. Laminated composites have raised interest for a long time for lightweight applications. However, manufacturing difficulties and limitations in mechanical properties have prevented a widespread usage. In fact, draping multiple two-dimensional plies in a mold of complex shape is difficult and low resistance to delamination [1, 2] remains a source of problems in structural parts. On the other hand, 3D engineering textiles woven to the shape of a complex part can be injected in a mold to manufacture net shape and thick components [3]. Moreover, the presence of a weave through the thickness prevents delamination.

The ply to ply interlock is one of the most remarkable 3D reinforcement [4, 5]. As shown in Fig. 1, its weaving architecture is particular: several layers of weft tows are joined in the warp direction and through the thickness by the warp tows. This kind of reinforcement has no third tow in the transverse direction. Three-dimensional interlock fabrics were devised specifically for high performance structural composite applications.

The physical phenomena that govern the manufacture of composite materials by resin injection are well known in LCM processes. Mold filling simulations are commonly used to optimize the injection process. However, this kind of simulation requires a good knowledge of material properties and particularly of a key parameter, the permeability of the fibrous reinforcement. Numerous experimental investigations have been carried out on permeability. Several models have also been

proposed in the scientific literature. However, because of the wide variety of fibrous reinforcements, it is difficult to predict permeability with a unique formula. Moreover, the stochastic feature of nesting, a phenomenon occurring in 2D laminate stacks and consisting of an interpenetration of fiber tows between neighboring plies [6], makes it difficult to come up with a general permeability model. Thus it is necessary to rely on experiments and so far only empirical models have been able to predict permeability with enough accuracy as a function of fiber volume fraction for various kinds of fibrous reinforcement.

The good control of weaving parameters in three-dimensional fabrics opens up the possibility of conducting more reproducible experiments, as well as interpreting more easily the results and thus determining appropriate models. Indeed, on the contrary to two-dimensional laminate stacks, the three-dimensional weaving pattern prevents any lateral displacement of the plies during the preforming stage. This means that no nesting occurs. Hence, the columns of tows remain aligned through the thickness of the fabric even if the reinforcement is highly compressed [7]. Consequently inter-tow macroscopic pores are present in the whole fabrics and create flow preferential channels along the tows. These open channels allow the test liquid to flow more easily in this kind of fabric than in laminates. Hence, the macroscopic pores can be assumed to be the main source of the pressure drop. As a matter of fact, when liquid resin is injected under pressure such as in the Resin Transfer Molding (RTM) process, the macroscopic (viscous) flow between the tows usually moves forward ahead of the microscopic (capillary) flow in the tows.

Researchers like Parnas et al. [8] have reported on the high reproducibility of in-plane and through-thickness permeability measurements for 3D reinforcement. Numerical predictions [9-11] of the in-plane permeability of 3D fabrics have also been carried out, but are still not accurate. Endruweit and Long [12] attempted to evaluate experimentally the influence of weaving parameters on the permeability of various 3D fabrics, but the fabrics tested were too different to allow constructing a general model.

The aim of this investigation is to understand how the macroscopic pores contained in the woven structure of three-dimensional interlock fabrics affect permeability, and thus derive a simple analytical predictive model. The study was conducted in three main stages:

1. Firstly, unidirectional permeability measurements are carried out in three in-plane directions for three different fabrics in order to evaluate the anisotropic permeability tensor and derive the so-called permeability ellipse [13].
2. The experimental results are then compared to understand how the test liquid flows through the fibrous reinforcements. A quantitative analysis is also carried out to evaluate the average size and distribution of the macroscopic pores in the tested fabrics.
3. Finally, a model derived from the calculation of the pressure drop in non circular ducts is created. The experimental data compiled in the two previous stages allow calculating and comparing predicted permeability values with experimental ones.

2. Description of experiments

2.1. Fabric specifications

Three three-dimensional interlock fabrics of areal density 11770 g/m² (Fabric 1), 14 564 g/m² (Fabric 2) and 11686 g/m² (Fabric 3) were selected to analyze the influence of weaving parameters on permeability. These fabrics possess the same weaving pattern, the same number of interlock plies (8 layers) and are made of the same kind of carbon fibers. Each of the 8 plies is composed of intersecting warp and weft tows superposed through the thickness of the fabric.

The only different weaving parameter between Fabric 1 and Fabric 2 is the warp/weft ratio. This means that the overall distribution of fibers is different. For example, a ratio of 60C/40T means

that 60% of the mass is distributed along the warp and 40% along the weft. However, these fabrics are composed of the same kind of tows, i.e., with the same number of filaments per tow and have the same warp tow count by ply n_{wp} (number of tows in the warp direction by centimeter). Thus, as shown in Tab. 1, the difference in directional fiber volume fraction is achieved by increasing or decreasing the number of tows in the weft direction (i.e., changing the weft tow count n_{wt} from the maximal tow count n_{max}). This parameter together with the warp tow count are weaving parameters characteristic of the structure of a given family of interlock fabrics. Tab. 1 below specifies the relationships between the tow counts for the fabrics.

On the other hand, the only difference between Fabric 1 and Fabric 3 is the number of filaments of the fiber tows in the weft direction. Fabric 3 has weft tows composed of 72 000 fibers instead of 48 000 for Fabric 1. The identical warp/weft ratio and the same warp tow count means that the distance between the heavier weft tows of Fabric 3 is larger than in Fabric 1. Hence, as displayed in Tab. 1, the weft tow count in Fabric 3 is lower than in Fabric 1.

2.2. Permeability measurement

The permeability K of a fibrous reinforcement is determined using Darcy's law [14], which in the unidirectional case connects the velocity of the fluid v_x with the pressure gradient $\partial P/\partial x$ and the dynamic viscosity μ :

$$v_x = \frac{-K}{\mu} \frac{\partial P}{\partial x} \quad (1)$$

Permeability was measured in a unidirectional flow experiment consisting of filling a rectangular RTM mold with a test liquid of known viscosity. The liquid was injected at a constant pressure of 1 bar and its velocity in time was measured by tracking the position of the flow front. For each measurement, the unidirectional permeability is calculated following the approach published by Ferland et al. [15]. Three series of measurements are necessary to obtain the in-plane permeability ellipse (see Fig. 2 for an example of such ellipse in a radial injection). As described in Demaria et al. [13], tests were conducted along the warp, weft and 45° directions. The cavity thickness of the mold was

adjusted with calibrated frames to achieve a fiber volume fraction of 58% for each reinforcement.

The test liquid is calibrated silicon oil from Dow Corning with a viscosity of 50 cSt. The Newtonian behavior of this fluid was verified with an Anton Paar rheometer. This fluid was chosen because its viscosity is close to that of a typical aeronautical RTM resin at high temperature.

2.3. Fabrication setup

In order to understand how the liquid flows through the fibrous reinforcement, a series of fabric samples were locked by injecting a polymeric resin, and then cut along the warp and weft directions in order to analyze the pore size and distribution. For each reinforcement, samples of 100*100 mm² were injected in a RTM mold at constant pressure with the vinylester resin Derakane 411-350 from Ashland Inc. The thickness was controlled by calibrated shims set in the mold to get the same fiber volume fraction as in the permeability tests. In order to reduce the quantity of voids in the final parts, resin was left bleeding during a few minutes [16, 17], after which a consolidation pressure of 3 bars is applied in the mold [18]. After demolding, the injected parts were cut into thin lamellas following a tow along the warp and weft directions. The cut-out surfaces were polished and analyzed with a digital microscope in order to evaluate the dimensions of the cross-section of the macroscopic pores (height, width, area). For each fabric and each warp or weft direction, six lamellas were prepared from two different fabricated parts.

3. Permeability results

Tab. 2 gives the effective permeability in the three directions tested for the three fabrics considered. Each permeability represents the average value of three tests. The standard deviation is displayed in brackets.

3.1. Influence of the warp/weft ratio

Fabrics 1 and 2 have a different warp/weft ratio. Fig. 3 and 4 show respectively the in-plane permeability ellipses obtained for Fabrics 1 and 2. The large and small axes of these ellipses are defined respectively as the square root of the two principal in-plane permeability values K_1 and K_2 , derived from the effective permeability following the methodology

described in Demaria et al. [13]. Fabric 1 is clearly anisotropic with an ellipse orientation angle of about 40°. Fabric 2 is less anisotropic; the orientation of its ellipse is almost the same as for Fabric 1. Comparing in Tab. 2 the experimental data in each direction for these two fabrics, it appears that the principal difference concerns the permeability at 90°; the permeability at 0° and 45° are close given the scatter of the measurements in terms of the standard deviation.

Each fabric has the same warp tow count (i.e., the same quantity of fibers along the warp), whereas in the weft direction Fabric 1 has a lower tow count (i.e., less fibers). This means that the macroscopic pores along the warp have probably the same width for both fabrics, while in the weft direction these pores are wider in Fabric 1. Moreover, Fabric 1 has a lower areal density. Thus, in order to obtain a comparable fiber volume fraction for each reinforcement, the mold cavity (i.e., the reinforcement thickness) must be lower for this fabric. This indicates that the macroscopic pores along the warp and weft in Fabric 1 have possibly a smaller height than in Fabric 2. Thus it seems consistent that the permeability values in the warp direction are close for both fabrics, because their pore sizes are slightly similar. In the weft direction, the pores of Fabric 1 have a smaller height and they are significantly larger than in Fabric 2. The permeability results show that this difference facilitates the liquid to flow in this direction.

3.2. Influence of the size of the fiber tows

Fig. 5 displays the in-plane permeability ellipse of Fabric 3. The same anisotropy as in Fabric 1 is observed. However, the ellipse is almost oriented in the weft direction. When we compare in Tab. 2 the experimental values of K_0 and K_{90} for Fabrics 1 and 3, it appears that this change comes principally from a difference of permeability in the warp direction. In fact, the warp permeability of Fabric 1 is two times higher than that of Fabric 3 while the weft permeability values are similar. This means that the flow in the warp direction is strongly affected by the presence of the 72K weft tows. These tows seem to form walls preventing the liquid from flowing from one macroscopic pore channel to another. Since the areal density are almost identical for these fabrics (i.e., the fabric thickness at $V_f = 58\%$ is nearly the

same), the height of the macroscopic pores has to be comparable. However, larger 78K fiber tows occupy more space than 48K tows. So the macroscopic pore channels are probably more squeezed in Fabric 3, thereby causing the significant reduction in permeability observed in Fig. 5 in the warp direction.

In the weft direction, Fabric 1 has a higher number of macroscopic pores than Fabric 3. However, the tow count indicates that these pores are certainly thinner. The total volume of macroscopic pores in this direction must be identical because both reinforcements possess the same warp/weft ratio and the same warp tow count. Moreover, K_{90} for Fabrics 1 and 3 are nearly identical. It means in this case that, the liquid flows with the same ease in a high number of thinner pores than in a smaller number of wider pores while the total volume of macroscopic pores is identical.

4. Analysis of pore size and distribution

4.1. Effective pore distribution

The aim here is to determine the average pore size and distribution for each fabric in each direction at a fiber volume fraction of 58%. As shown in Fig. 6, the lamellas fabricated permit to observe and analyse the macroscopic pore size and distribution in each fabric along the warp and weft directions. Pores at 45° are not studied here because they result from complex combination of warp and weft channels. However, permeability could be assessed in any direction by studying the liquid flow through the whole porous network.

As observed in the example of Fig. 6, the pore distribution of a 3D interlock fabric is well defined. Despite compaction of the reinforcement at 58% fiber volume content, fiber tows (in black) still remain in their in-plane initial positions. In this example, it is also possible to identify the unit cell. Indeed, the column of tows number 9 is the repetition of column 1. The pore distribution was mapped for each lamella and a microscopic analysis of each pore was carried out to determine their size.

4.2. Pore analysis and modeling

The numerous pore cross-sections have various shapes. However, the particular organisation of this kind of fabric resulted in a nearly rectangular shape for most of them; hence it seems natural to fit these

cross-sections by an equivalent rectangle of identical area. An equivalent circular or elliptical channel could also have been selected. However, it was found more appropriate to remain as close as possible to the shape of the existing channels. Thus each pore will be defined by the semi-height h_c and semi-width w_c of its equivalent rectangle as shown in Fig. 7.

In order to obtain the mean pore size (i.e., the mean rectangle) of the fabrics in each direction, it is necessary to analyze the images acquired with the microscope. A Matlab routine was created to firstly process the raw images (Fig. 8a to 8b), and then to fit the rectangular shape (Fig. 8c). The fitted rectangle is calculated by the least-square method. The area of the rectangle is identical to that of the pore. This procedure was applied to each lamella (6 lamellas for each fabric in each direction) in order to determine the height, width and area of the pores. An example of pore size identification is shown in Fig. 9 for a lamella of Fabric 1.

It is now possible to calculate the average pore size and distribution in each direction of the fabrics considered. This information will then be used to model with an analytical solution of Stokes equation the liquid flow through the fibrous reinforcement.

5. Poiseuille flow in a rectangular cross-section channel

A fully developed flow of an incompressible Newtonian liquid in a long channel of rectangular cross-section is governed by the following Poisson equation:

$$\frac{\partial^2 v_x}{\partial y^2} + \frac{\partial^2 v_x}{\partial z^2} = \frac{1}{\mu} \frac{\partial p}{\partial x} \quad (2)$$

The symmetry with respect to the planes $y = 0$ and $z = 0$ displayed in Fig. 7 permits to develop equation (2) for only one quarter of the channel. In this case, the boundary conditions can be written as follows:

$$\text{when } \begin{cases} y = 0, & \frac{\partial v_x}{\partial y} = 0 \\ y = w_c, & v_x = 0 \\ z = 0, & \frac{\partial v_x}{\partial z} = 0 \\ z = h_c, & v_x = 0 \end{cases} \quad (3)$$

Since $\partial P/\partial x$ is not function of y or z , equation (2) can be satisfied only when $\partial P/\partial x$ is constant. This term can be eliminated by introducing a new dependent variable v'_x which satisfies the Laplace equation. Thus, equation (2) can be transformed by setting:

$$v_x(y, z) = -\frac{1}{2\mu} \frac{\partial P}{\partial x} (h_c^2 - z^2) + v'_x(y, z) \quad (4)$$

with v'_x constant on the wall. Substituting equation (4) into equations (2) and (3), we get:

$$\frac{\partial^2 v'_x}{\partial y^2} + \frac{\partial^2 v'_x}{\partial z^2} = 0 \quad (5)$$

with the following boundary conditions:

$$\text{when } \begin{cases} y = 0, & \frac{\partial v'_x}{\partial y} = 0 \\ y = w_c, & v'_x = \frac{1}{2\mu} \frac{\partial P}{\partial x} (h_c^2 - z^2) \\ z = 0, & \frac{\partial v'_x}{\partial z} = 0 \\ z = h_c, & v'_x = 0 \end{cases} \quad (6)$$

The above problem can be solved using the principle of separation of variables. After various substitutions, the fluid velocity is:

$$v_x(y, z) = -\frac{1}{2\mu} \frac{\partial P}{\partial x} h_c^2 \left[1 - \left(\frac{z}{h_c} \right)^2 + \frac{32}{\pi^3} \sum_{i=1,3,5,\dots}^{\infty} (-1)^{(i-1)/2} \frac{\cosh\left(\frac{i\pi y}{2h_c}\right)}{\cosh\left(\frac{i\pi w_c}{2h_c}\right)} \cos\left(\frac{i\pi z}{2h_c}\right) \right] \quad (7)$$

Finally, by integrating the velocity profile described in equation (7) over the rectangular cross-section, the volumetric flow rate Q can be calculated as follows:

$$Q = -\frac{4 \cdot w_c \cdot h_c^3}{3 \cdot \mu} \left(\frac{\partial P}{\partial x} \right) s \quad (8)$$

where

$$s = \left(1 - \frac{192 \cdot h_c}{\pi^5 \cdot w_c} \sum_{i=1,3,5,\dots}^{\infty} \frac{\tanh(i\pi w_c/2h_c)}{i^5} \right) \quad (9)$$

6. Permeability calculation

Considering now the liquid flowing through a fibrous reinforcement, the velocity can be calculated as a function of the number of pores n_c and the mean pore dimension:

$$v_x = \frac{Q}{4 \cdot n_c \cdot h_c \cdot w_c} \quad (10)$$

Replacing equation (10) in equation (8) and integrating, the pressure drop becomes:

$$\Delta P = \frac{3 \cdot C \cdot v_x \cdot \mu \cdot l_c}{h_c^2 \cdot s} \quad (11)$$

where C is a dimensionless shape factor and l_c the length of the channel. C is calculated from the ratio between the pressure drop in a rectangular channel and in a real shape channel. l_c can be calculated from the length of the fabric sample l_f , the channel tortuosity τ_c and the ratio between the tow count in the direction perpendicular to the flow and the maximum possible tow count r_t (in the same direction):

$$l_c = \frac{l_f \cdot \tau_c}{r_t} \quad (12)$$

As explained in the introduction, macroscopic pores are present along the tows. Thus the channel tortuosity is assumed to be equal to the tortuosity of the tows. The parameter r_t permits to correct the total length of the channel (i.e. $l_f \cdot \tau_c$) to the length really responsible for the pressure drop. In fact, when tows perpendicular to the flow are not in contact, each channel is divided in multiple sections connected between them by free spaces as shown in Fig. 10, in which there is no pressure drop. The real length l_c of the channels with pressure drop is thus the sum of the sections in the defined direction. It can be calculated by dividing the total length by the ratio r_t .

Finally, by integrating equation (1) (when the velocity of the injected fluid is constant), the permeability becomes:

$$K = \frac{Q \cdot \mu \cdot l_f}{h_f \cdot w_f \cdot \Delta P} \quad (13)$$

where h_f and w_f are respectively the thickness and the width of the fabric sample. This equation permits to connect directly the permeability of three-dimensional fabrics with the pore size, the distribution of the pores in a given direction and the characteristic tortuosity of the woven structure of the fabric.

7. Results

7.1. Effective permeability calculation

Using the dimensions of the macroscopic pores obtained by the microscopic analysis and the weaving parameters, equation (11) and (13) permits to calculate the effective permeability in the warp and weft directions of the 3D fabrics investigated. As explained in the previous section, the permeability at 45° is not calculated here because the macroscopic pores are a complex combination of warp and weft channels. In order to obtain this value, it is necessary to model the liquid flow through the whole fabric, and not only in a channel. Fig. 11 and 12 present the comparison between the experimental and calculated permeability in the warp (0°) and weft (90°) directions respectively. A good correlation is observed in both directions. These results mean that the permeability model (13) is well representative of the fluid flow in the fibrous reinforcements considered.

7.2. Prediction of in-plane permeability ellipses

In order to obtain the in-plane permeability ellipse, it is necessary to determine either another value of permeability in a third direction or the angle between the major axis of the ellipse and the warp direction, namely the so-called θ angle. Our approach is based on the existence of continuous oriented channels along the two weaving directions, i.e. warp and weft. There is thus *a priori* no third channel orientation in the plane of the fabric. This can make the determination of the angle θ simpler. This angle can be hypothetically derived from parameters of the fabric architecture. From the experimental permeability results obtained earlier for these kinds of fabric, the ratio of the warp over the weft tow counts is assumed to play a significant role (if other weaving parameters are similar), so that the following hypothesis can be emitted: if $n_{wp}/n_{wt} > 2$, the flow is clearly promoted in the

weft direction; on the contrary, if $n_{wp}/n_{wt} < 0.5$, the flow will take place mainly in the warp direction. In these specific cases, the ellipse will be oriented respectively along the weft ($\theta = 90^\circ$) or along the warp ($\theta = 0^\circ$). Based on this assumption, the ellipse orientation of Fabric 3 is defined as 90° .

Fabrics 1 and 2 are not in this configuration. However, any identical woven fabric with a warp/weft ratio of 70C/30T will be. Thus the corresponding ellipse orientation will also be 90° . Then interpolating these values of θ for the real warp/weft ratio of Fabrics 1 and 2 leads to:

$$\theta = \frac{\pi \cdot n_{wp}}{2 \cdot n_{wt}} \quad (14)$$

which gives an orientation of the permeability ellipse of 60° for Fabric 1 and 38.6° for Fabric 2. Once the value of K_0 , K_{90} and θ are known, the principal permeability values K_1 and K_2 can be calculated by the formula [13]:

$$K_1 = \frac{2 \cdot K_0 \cdot K_{90}}{K_0 + K_{90} - (K_0 - K_{90}) \cdot \cos(2\theta)} \quad (15)$$

and

$$K_2 = \frac{2 \cdot K_0 \cdot K_{90}}{K_0 + K_{90} + (K_0 - K_{90}) \cdot \cos(2\theta)} \quad (16)$$

Finally, in-plane permeability ellipses can be drawn. Fig. 13, 14 and 15 show the predicted ellipses (plain line) compared to the measured ones (dotted line) for Fabrics 1, 2 and 3 respectively. A good correlation is observed in the three cases.

8. Conclusion

The permeability of three three-dimensional interlock fabrics with different weaving parameters was measured by unidirectional injections carried out at constant pressure in a rectangular test mold. In a first analysis of the experimental results, the weaving parameters appeared to be connected with the liquid flow behavior. Based on this affirmation and on the architecture of the 3D woven fabrics, the macroscopic pores were identified as the main source of pressure drop in a RTM injection. The macroscopic pore size and distribution were investigated via a microscopic analysis conducted on lamellas cut out from composite samples fabricated

by resin injection. An average pore size was then calculated for each fabric in the warp and weft directions.

In parallel, a model derived from the exact solution of the pressure drop of a liquid flowing in a rectangular channel was created. This model was adapted for the specific case of 3D interlock fabrics in order to connect the predicted directional permeability to the pore size, the distribution of pores and their tortuosity. This model was then applied in the warp and weft directions to the three fabrics considered using data collected from the microscopic analysis. A good correlation between predicted and experimental results was obtained for permeability in the warp and weft directions.

The orientation of the in-plane permeability ellipse was also predicted as a function of the warp over weft tow count. This allowed calculating the principal permeability tensor for each fabric. A good correlation was also observed between the experimental and predicted permeability ellipses. This analysis shows that the permeability of 3D interlock fabrics can be predicted. However, the macroscopic pore size and distribution have to be determined. The next step of this investigation would be to find the relationship between the weaving parameters and the pore properties in order to predict the permeability without any experimental analysis. Finally, this model could possibly be generalized to other kinds of 3D reinforcements.

9. Acknowledgements

The authors are grateful to Safran who funded this investigation and provided the fibrous reinforcements used in the experiments. The contributions of the National Science and Engineering Research Council (NSERC) of Canada, of the Fonds Québécois pour la Recherche sur la Nature et les Technologies (FQRNT), of the Canada Foundation for Innovation (CFI) and of the Ministère de l'Éducation du Québec for the research infrastructure are also gratefully acknowledged. Authors would like also to thank especially T. Godon from Snecma, France, and S. Oger from Conservatoire National des Arts et Métiers (CNAM), Paris, France for their technical support.

10. References

- [1] Huimin, F. and Yongbo, Z., "On the distribution of delamination in composite structures and compressive strength prediction for laminates with embedded delaminations", pp. 1-17, 2010.
- [2] Perrot, Y., Davies, P., Kerboul, A., and Baley, C., "Marine composites based on low styrene content resins. influence of lamination procedure and peel plies on interlaminar resistance", *Applied Composite Materials*, vol. 15, pp. 87-97, 2008.
- [3] Mouritz, A. P., Bannister, M. K., Falzon, P. J., and Leong, K. H., "Review of applications for advanced three-dimensional fibre textile composites", *Composites Part A: Applied Science and Manufacturing*, vol. 30, pp. 1445-1461, 1999.
- [4] Ansar, M., Xinwei, W., and Chouwei, Z., "Modeling strategies of 3D woven composites: A review", 2011.
- [5] Younes, R. and Zaki, W., "Optimal weaving for 2.5D interlocks", *Composite Structures*, vol. 93, pp. 1255-1264, 2011.
- [6] Hoes, K., Dinescu, D., Sol, H., Parnas, R. S., and Lomov, S., "Study of nesting induced scatter of permeability values in layered reinforcement fabrics", *Composites Part A: Applied Science and Manufacturing*, vol. 35, pp. 1407-1418, 2004.
- [7] Karahan, M., Lomov, S. V., Bogdanovich, A., Mungalov, D., and Verpoest, I., "Internal geometry evaluation of non-crimp 3D orthogonal woven carbon fabric composite", *Composites Part A: Applied Science and Manufacturing*, 2010. En attente de publication.
- [8] Parnas, R. S., Flynn, K. M., and Dal-Favero, M. E., "A permeability database for composites manufacturing", *Polymer Composites*, vol. 18, pp. 623-633, 1997.
- [9] Zeng, X. S., Endruweit, A., Long, A. C., and Clifford, M. J., "CFD flow simulation for impregnation of 3D woven reinforcements", in *10th International Conference on Textile*

- Composites: Recent Advances in Textile Composites, TEXCOMP 10, October 26, 2010 - October 28, 2010, Lille, France, 2010, pp. 455-462.*
- [10] Verleye, B., Croce, R., Griebel, M., Klitz, M., Lomov, S. V., Morren, G., Sol, H., Verpoest, I., and Roose, D., "Permeability of textile reinforcements: Simulation, influence of shear and validation", *Composites Science and Technology*, vol. 68, pp. 2804-2810, 2008.
 - [11] Verpoest, I. and Lomov, S. V., "Virtual textile composites software WiseTex: Integration with micro-mechanical, permeability and structural analysis", *Composites Science and Technology*, vol. 65, pp. 2563-74, 2005.
 - [12] Endruweit, A. and Long, A. C., "Analysis of compressibility and permeability of selected 3D woven reinforcements", *Journal of Composite Materials*, vol. 44, pp. 2833-2862, 2010.
 - [13] Demaria, C., Ruiz, E., and Trochu, F., "In-plane anisotropic permeability characterization of deformed woven fabrics by unidirectional injection. Part I: Experimental results", *Polymer Composites*, vol. 28, pp. 797-811, December 2007 2007.
 - [14] Darcy, H., *The public fountains of the city of Dijon*. Paris: Dalmont, 1856.
 - [15] Ferland, P., Guittard, D., and Trochu, F., "Concurrent methods for permeability measurement in resin transfer molding", *Polymer Composites*, vol. 17, pp. 149-158, 1996.
 - [16] Lundstrom, T. S., "Void formation in RTM", *Journal of Reinforced Plastics and Composites*, vol. 12, pp. 1339-1349, 1993.
 - [17] Labat, L., Breard, J., Pillut-Lesavre, S., and Bouquet, G., "Void fraction prevision in LCM parts", *EPJ Applied Physics*, vol. 16, pp. 157-164, 2001.
 - [18] Lundstrom, S. and Gebart, R., "Influence from process parameters on void formation in resin transfer molding", *Polymer Composites*, vol. 15, pp. 25-33, 1994.
 - [19] Endruweit, A., Long, A. C., Robitaille, F., and Rudd, C. D., "Influence of stochastic fibre angle variations on the permeability of bi-directional textile fabrics", *Composites Part A: Applied Science and Manufacturing*, vol. 37, pp. 122-132, 2006.

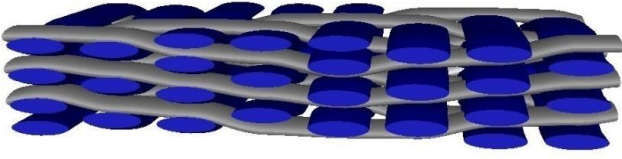


Fig. 1 – Example of 3D interlock fabric.

Tab. 1 - Details of fabric weaving parameters

	1	2	3
Areal density (g/m^2)	11770	14564	11686
Ratio warp/weft	60C/40T	50C/50T	60C/40T
Number of fibers/tow	48K/48K	48K/48K	48K/72K
Warp tow count (tows/cm/ply)	n_{max}	n_{max}	n_{max}
Weft tow count (tows/cm/ply)	$\frac{2}{3}n_{max}$	n_{max}	$\frac{4}{9}n_{max}$

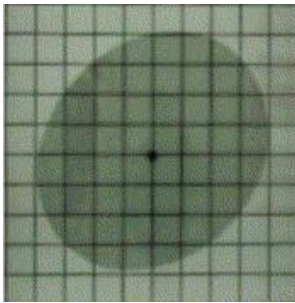


Fig. 2 – Satin weave in-plane permeability ellipse observed by Endruweit et al. [19].

Tab. 2 – Effective permeability results

	K_0	K_{45}	K_{90}
1	$1.62(\pm 0.23)e^{-10}$	$1.15(\pm 0.19)e^{-10}$	$1.96(\pm 0.25)e^{-10}$
2	$1.20(\pm 0.24)e^{-10}$	$1.35(\pm 0.19)e^{-10}$	$1.00(\pm 0.05)e^{-10}$
3	$0.75(\pm 0.11)e^{-10}$	$1.51(\pm 0.11)e^{-10}$	$2.18(\pm 0.61)e^{-10}$

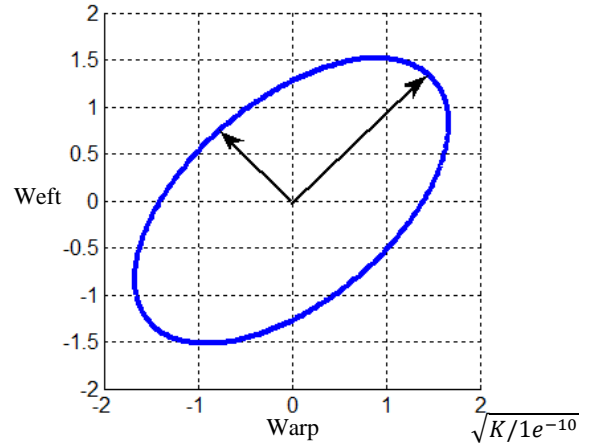


Fig. 3 – Measured in-plane permeability ellipse of Fabric 1.

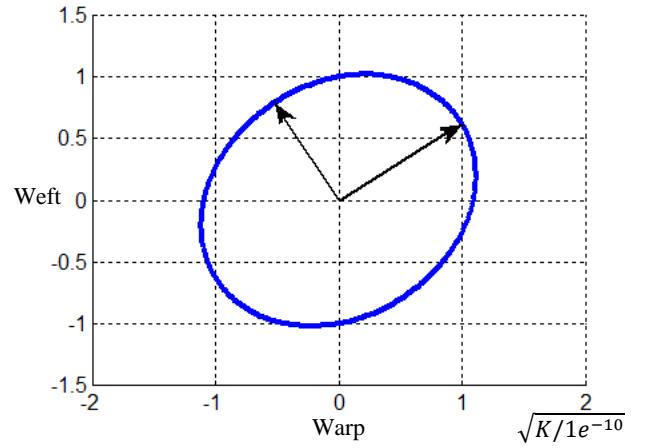


Fig. 4 – Measured in-plane permeability ellipse of Fabric 2.

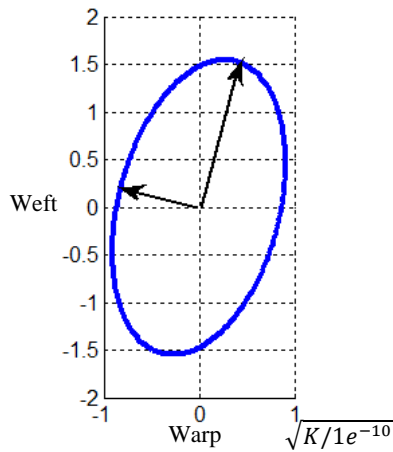


Fig. 5 – Measured in-plane permeability ellipse of Fabric 3.

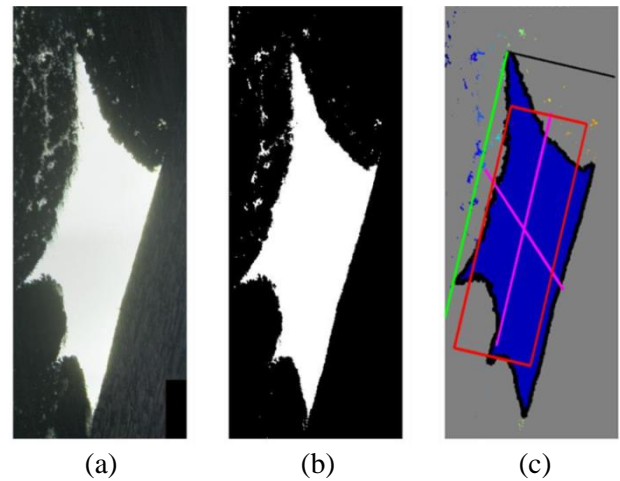


Fig. 8 – Pore image processing: (a) raw image, (b) processed image and (c) rectangular fit.

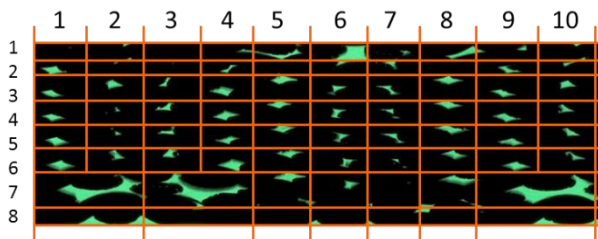


Fig. 6 – Mapping of part of a Fabric 1 lamella (vertical cross-section in a perpendicular direction to the weft).

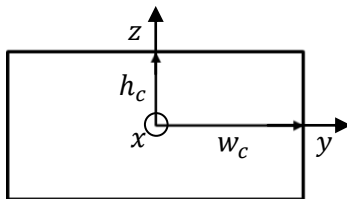


Fig. 7 – Definition of the equivalent pore channel 10 dimensions.

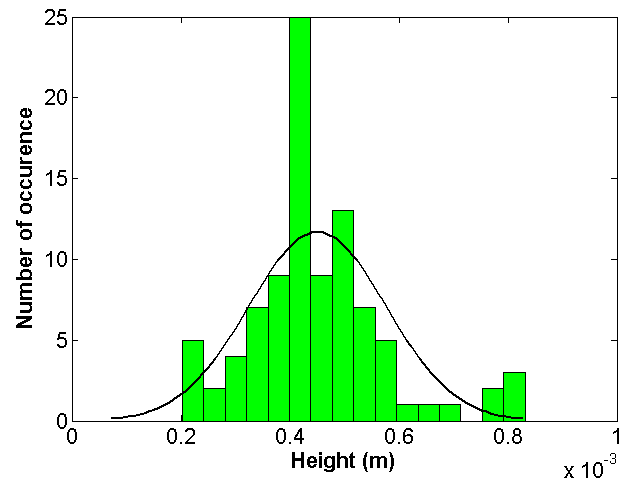


Fig. 9 – Pore height distribution obtained for a lamella of Fabric 1. The full line is the equivalent normal distribution.

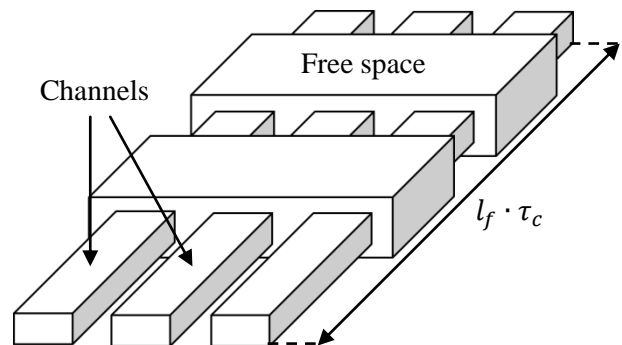


Fig. 10 – Connectivity of the pore channels.

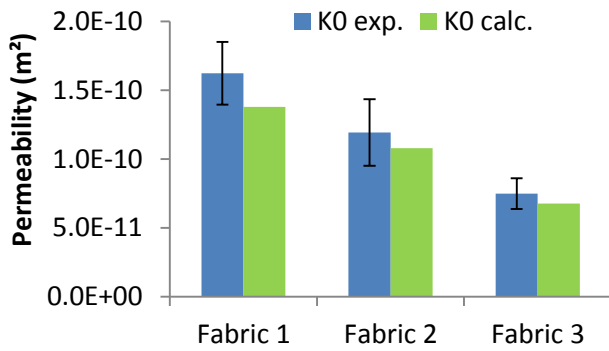


Fig. 11 – Measured and calculated effective permeability at 0°.

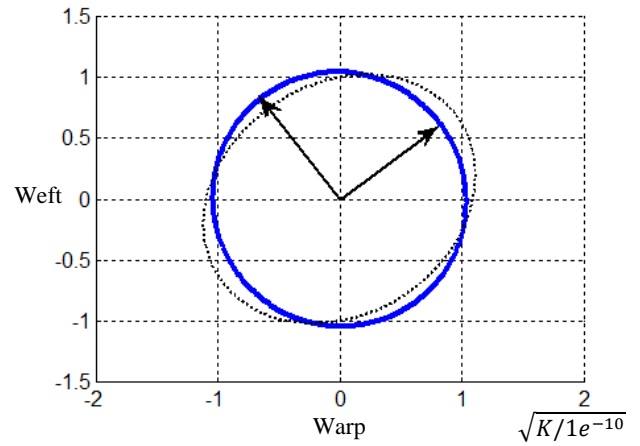


Fig. 14 – Predicted (plain line) and experimental (dotted line) permeability ellipses for Fabric 2.

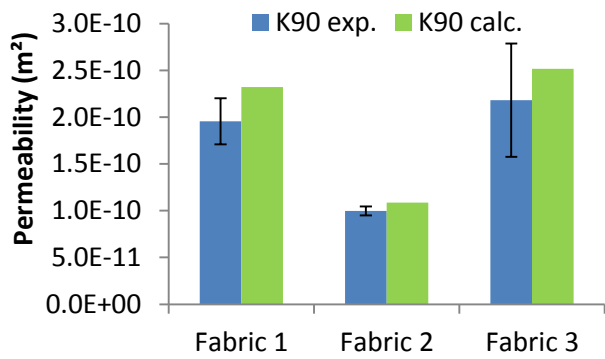


Fig. 12 – Measured and calculated effective permeability at 90°.

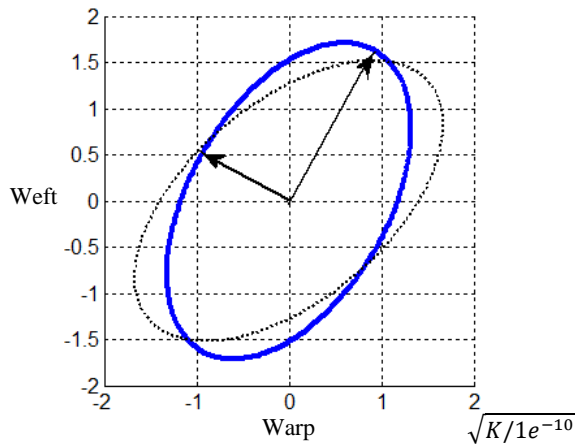


Fig. 13 – Predicted (plain line) and experimental (dotted line) permeability ellipses for Fabric 1.

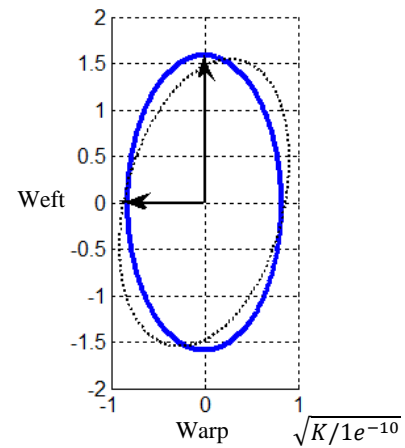


Fig. 15 – Predicted (plain line) and experimental (dotted line) permeability ellipses for Fabric 3.